This is the peer-reviewed, final accepted version for American Mineralogist, published by the Mineralogical Society of America.
The published version is subject to change. Cite as Authors (Year) Title. American Mineralogist, in press.
DOI: https://doi.org/10.2138/am-2022-7969. http://www.minsocam.org/

Revision 1

A Multi-faceted Experimental Study on the Dynamic Behavior of $MgSiO_3$ Glass in the Earth's Deep Interior.

Young Jay Ryu[1,*], Yanbin Wang[1], Tony Yu[1], Fiona Bonnet[1,†], Eran Greenberg[1,††], Clemens Prescher[2], Vitali B. Prakapenka[1], Sergey Tkachev[1], Peter Eng[1], Joanne E. Stubbs[1], Przemyslaw Dera[3], Heather Watson[4], and Mark L. Rivers[1]

[1]Center for Advanced Radiation Sources, The University of Chicago, Chicago, IL 60637, USA.

[2]Institute of Earth and Environmental Sciences, Albert-Ludwigs-Universität Freiburg, Freiburg, D-79104, Germany.

[3]Hawai'i Institute of Geophysics and Planetology, University of Hawai'i Mānoa, Hawai'i, HI, 96822, USA.

[4]Department of Physics and Astronomy, Union College, Schenectady, NY 12308, USA.

[†]Currently at the Laboratoire de Science de la Terre, CNRS UMR 5570, ENS Lyon, 46 allée d'Italie, 69634 Lyon cedex, 7, France.

[††]Currently at the Applied Physics Department, Soreq Nuclear Research Center (NRC), Yavne 81800, Israel.

*Corresponding author: ryu@cars.uchicago.edu (Y-J. Ryu)

Abstract

Pressure-induced structural modifications in silicate melts play a crucial role in controlling dynamic processes in deep interiors of the Earth and other planets. The correlation between structural and macroscopic properties of silicate liquids (densification, viscosity, chemical differentiation, etc.), however, remains poorly understood. Here we report the evolution of structural modifications and elastic properties of $MgSiO_3$ glass to pressures up to ~70 GPa using a combination of experimental techniques including micro-confocal Raman spectroscopy, angle dispersive X-ray scattering, and Brillouin spectroscopy in the diamond anvil cell. Our combined dataset provides consistent and complementary evidence of a series of pressure-induced structural modifications in $MgSiO_3$ glass at ~2, ~8, ~20, and ~40 GPa. Based on these results, a structural evolution model for $MgSiO_3$ glass is proposed. We also discuss the role of Mg-O component in $MgSiO_3$ and Mg_2SiO_4 glasses in controlling pressure-induced structural modifications and mechanical responses in these supercooled liquids.

Keywords: $MgSiO_3$ silicate glass under high-pressure, structural modification, Raman spectroscopy, Brillouin spectroscopy, X-ray scattering

Introduction

The present-day Earth possesses a crust composed of low-density minerals enriched in incompatible lithophile elements and a high-density metallic core beneath the rocky mantle, indicating that our planet is a well-differentiated body. Chemical differentiation of the mantle is generally attributed to melting and subsequent crystallization in the early Earth. It is believed

that the mantle underwent large-scale melting after the Moon-forming giant impact event (Agee and Walker, 1988; Ohtani, 1988). Materials with different chemical compositions were produced through melting, with incompatible elements partitioning preferentially into the melts, which were then separated by gravitational effects, forming the crust. High $^{142}Nd/^{144}Nd$ ratios in terrestrial samples relative to chondritic meteorites suggest an early enriched reservoir in the deep mantle (Boyet and Carlson, 2005). Such a magma ocean scenario, in turn, plays an important role in understanding the core formation process (Badro et al., 2015; Li and Agee, 1996). Deep mantle melting has been used to explain a wide range of seismic and geochemical observations. One example is the proposal that the ultralow velocity zone (ULVZ) in the D″ layer may represent a melt layer at the core-mantle boundary (Labrosse et al., 2007). Structural and physical properties of silicate melts under deep mantle conditions are required to understand the physics of deep melts and verify these hypotheses.

Experimental information on the structure, density, and compressibility of silicate liquids and glasses (super-cooled liquids) at high-pressure (HP) and high-temperature (HT) is vital in the evaluation of the deep magma ocean hypothesis and the related interpretations of geophysical observations. Considerable progress has been made over the past few decades in establishing the correlation between structure and properties (such as density and elasticity) of silicate liquids, at pressure up to ~5 or ~6 GPa. Recent molecular dynamics (MD) simulations have shown that the dominant effects of increasing density and bulk modulus are the closure of voids space in the structure at low pressure regime and the rearrangement of cation-oxygen bond length and angles, as well as changes in coordination environment at high pressures (Karki, 2010; Kubicki and Lasaga, 1988). Experimental studies on both silicate liquids and glasses show that, upon compression, the atomic arrangements become much more efficiently packed by increasing

cation-oxygen coordination numbers (CN), resulting in a significant density increase (McMillan, 1984; Meade and Jeanloz, 1988; Prescher et al., 2017).

$MgSiO_3$ is a major component in the Earth's upper mantle and the dominant constituent of the lower mantle. No direct information on $MgSiO_3$ liquid has been obtained experimentally under lower mantle conditions, because simultaneous HP and HT conditions impose severe technical challenges in the collection of structural and property data. Instead, $MgSiO_3$ glass, the supercooled liquid, is studied, in terms of the structure, density, and elasticity (Cormier and Cuello, 2011; Kono et al., 2018; Lee et al., 2008; Murakami and Bass, 2011; Petitgirard, 2017; Petitgirard et al., 2015; Sanchez-Valle and Bass, 2010; Shim and Catalli, 2009). In most previous studies, the focus was either on structure or certain physical properties. No direct correlation between structure and physical properties has been established. Furthermore, the previous studies have reported rather diverse results of pressure-induced structural modifications in $MgSiO_3$ glass. For instance, Kubicki et al. and Shim et al. suggested that significant structural modifications in local structure occur at 19-38 and 65-70 GPa based on the Raman studies (Kubicki et al., 1992; Shim and Catalli, 2009), whereas Lee et al. reported the formation of tri-cluster oxygen and changes in local coordination between 12 - 20 GPa and 40 GPa, respectively, based on the oxygen K-edge X-ray Raman measurements (Lee et al., 2008). Sanchez-Valle et al. recently reported that the structure of $MgSiO_3$ glass shows anomalous changes at 8 GPa and between 15 and 18 GPa, based on the Brillouin measurements (Sanchez-Valle and Bass, 2010). Recently, Ghosh et al, further reported the structural changes at 12 or 25 GPa based on the MD simulations (Ghosh et al., 2014). Additionally, several studies have been performed using neutron diffraction and NMR spectroscopy to evaluate the structure of high-pressure melts based on the structures of quenched metal oxide-silica glasses (Salmon et al., 2019; Sen et al., 2009;

Xue et al., 1991). In those glasses, the presence of higher-coordinated Si-O_x (x= 4) is primarily due to high pressure (>12 GPa) and high temperature (>1600°C), therefore the characteristics of the glasses are expected to be different than those in low-pressure glasses at room temperature. Our aim in this study is to understand how the low-pressure glasses respond to compression at ambient temperature. Thus, it is imperative to make adjustments and demonstrate a complete and consistent scope for pressure-induced structural modification in $MgSiO_3$ glass. Here we take a multifaceted experimental approach to study $MgSiO_3$ glass by using Raman spectroscopy, angle dispersive X-ray scattering, and Brillouin spectroscopy, to examine the connection between structure and macroscopic properties of this super-cooled liquid. Raman spectroscopy is widely used for probing vibrations of molecules and structural units in both crystalline and amorphous materials and is highly sensitive to local interactions among various cation-anion groups. X-ray diffraction, on the other hand, gives average distances between neighboring atoms over the diffracting volume. The two techniques complement each other to provide both quantitative and qualitative interpretation regarding the atomic arrangements. Brillouin spectroscopy senses high-frequency (non-relaxed) elastic properties of the sample during structural changes under high pressure. The detailed structural and property data, collected on the same sample in the same diamond-anvil cell, allow us to gain first-hand information as to how structural changes affect physical properties and uncover missing links between the structure and physical property relationships, thus helping place better constraints on dynamic behaviors of silicate liquids within the Earth's deep interior. Furthermore, a knowledge of structural evolution in silicate glasses at high pressure may help elucidate the nature of chemical differentiation processes and facilitate synthesis of more advanced technological materials used in various fields such as optics, electronic insulators, and storage for nuclear wastes.

Experimental methods

Materials synthesis

Reagent-grade oxides [MgO (99.99%) and SiO_2 (99.9%)] crystalline powders were purchased from Sigma-Aldrich. Stoichiometric MgO and SiO_2 powders (molar ratio 1:1) were carefully comminuted to micron-sized particles by impregnation using a small portion of ethanol for 4 hours in a glove box flushed with inert argon (Ar) gas. The binary mixture was thoroughly dried in a custom designed high vacuum heating device at 390 K for 48 hours. As shown in Figure S2A, the Raman spectrum does not show any contamination in the binary mixture (MgO + SiO_2), demonstrating a nearly pure $MgSiO_3$ composition. High-pressure and high-temperature synthesis of $MgSiO_3$ glass was conducted using the Paris-Edinburgh large volume press (VX-5: MG63) of the Geo-Soil-Enviro Center for Advanced Radiation Sources (GSECARS) Beamline 13-ID-C at the Advanced Photon Source (APS), Argonne National Laboratory (ANL). Tungsten carbide (WC) anvils were used to generate high pressure (up to 1 GPa). The cell assembly used is shown in Figs. S1A and S1B. Pressure was manually controlled by varying the hydraulic ram load while heating and cooling of the cell assembly were accomplished through a proportional-integral-derivative (PID) feedback control. The magnesium oxide (MgO) sleeve surrounding the sample capsule was used as the pressure calibrant. The sample pressure was determined based on the pressure-volume-temperature (P-V-T) equation of state of MgO (Speziale et al., 2001). Temperature was generated by resistive heating up to 2000 K and estimated according to pre-calibrated power versus temperature relationship. Particular attention was paid to the homogeneity of the "pseudo-binary" liquids, by maintaining temperature sufficiently above the

melting point of $MgSiO_3$ to ensure complete and homogeneous melting. The melt was then quenched to ambient temperature by super-cooling. X-ray scattering, Raman spectroscopy and optical microscopy techniques were used to verify the homogeneity of the glass sample. The optical microphotograph image of the recovered $MgSiO_3$ glass sample (Figs. S1C, S1D) shows that the glass is highly transparent and possess a glassy surface. The sample thus synthesized is a pure $MgSiO_3$ glass, as no signatures of crystalline forsterite (Mg_2SiO_4) or hydrous enstatite [$Mg(OH)_2$ + H_2SiO_3], whose major Raman bands are located around 880 and 3300 cm^{-1}, respectively, can be detected. In addition, we also synthesized silica (SiO_2) glass to perform Raman measurements for comparison with $MgSiO_3$ glass at ambient conditions (Fig. S2C).

Raman Characterization

The confocal micro-Raman system at GSECARS (Holtgrewe et al., 2019) was used to investigate the vibrational spectra of the recovered (from ~1 GPa and ~ 2000 K) $MgSiO_3$ glass sample. The Raman system (3μm spatial and 5 cm^{-1} spectral resolution, and 3 μm laser beam size at the focal point) is equipped with a spectrometer (Acton SpectraPro SP-2500, Princeton Instrument; 1800, 1200, and 300 grooves per mm grating), a holographic diffractive bandpass filter (Semrock), and a Raman notch filter (OptiGate). The system is operated in a back-scattering configuration, using an apochromatic objective lens (20x, 30.5 mm working distance, Mitutoyo) and a 50 μm confocal pinhole to collect the spatially filtered back-scattered Raman radiation only from the region of interest. To avoid detrimental effects of photo-damage and fluorescence on the sample, excitation wavelengths of 532 nm and 660 nm were employed with a coherent laser (Verdi V2) and Laser Quantum, respectively, with a power of less than 20 mW. The recovered $MgSiO_3$ glass was loaded in both symmetric and BX-90 diamond anvil cells

(Princeton) and pressurized (in 2 GPa steps) in non-hydrostatic and hydrostatic conditions with neon (Ne) as a pressure medium. However, we found that the non-hydrostatic condition provides a less scattering effect from the diamond and no artificial discontinuities from the pressure media, thus we only describe the measurement in non-hydrostatic conditions in this present study. The Raman spectra of $MgSiO_3$ glass were recorded in a range of 0 to 1300 cm^{-1}, with various exposure times (from 600 to 3600 seconds) at room temperature (300 K). In addition, we compared the sample recovered from high-pressures and temperature (~1 GPa, 2000 K) with the sample obtained by using the levitation technique (0 GPa, 2000 K), and both showed the same Raman frequencies within an uncertainty of ± 5 cm^{-1}. A >5 μm-sized single crystal spherical ruby was loaded into the cell for pressure determination (see Fig. S7A) (Dewaele et al., 2008). Type IA diamond anvils with a culet size of 0.3 mm were used. The pressure determination above 25 GPa was based on the diamond band of Raman edge line (see Fig. S7B) (Akahama and Kawamura, 2006). All of the collected Raman spectra were analyzed and spectral fitting was conducted using Fityk (Wojdyr, 2010). In order to carry out further spectral analysis, the background was subtracted from the baseline (Fig. S3), and Gaussian + Lorentzian line shape distribution functions were applied to deconvolute the spectra by using the XPS peakfit 4.1 software. It should be noted that the background subtraction is done with careful execution. In our analysis, we first collected Raman spectrum from an empty DAC and removed the background using the T-rax program *prior to* subtracting the background of each spectrum (Fig. S3). Then the background was fitted with a polynomial function and subtracted. This approach has minimized artifacts due to background subtraction.

Synchrotron X-ray scattering measurement

The high-pressure X-ray scattering experiments were performed at the 13-IDD beamline (GSECARS, APS, ANL). In order to generate pressure on the $MgSiO_3$ glass up to 72 GPa, both BX-90 and symmetric diamond anvil cells (DAC; Princeton) were used and all measurements were performed at room temperature (300 K). An incident monochromatic X-ray beam which was produced by a Si-111 single crystal monochromator with a maximum energy of 42 keV and a 3 μm x 4 μm beam size was used. A multi-channel collimator (MCC) described in previous works (Prescher et al., 2017; Yu et al., 2019) with a 50 μm inner slit size and 200 μm outer slit size was used for all measurements. Type-IA diamond anvils with 0.25- and 0.3 mm culet sizes were used. Similar to the aforementioned sample synthesis procedure, the $MgSiO_3$ glass was ground into fine glass powder and loaded into the pressure chamber in a Re gasket. No pressure medium was used to avoid any scattering effects from the diamond and artificial discontinuities from the pressure media. To enhance the reliability of pressure measurements, a <5μm diameter piece of gold (Au) foil (2 μm thick) was used as a pressure calibrant. X-ray diffraction of the Au piece was collected before and after each structure measurement to determine the pressure based on the known equation of state of Au (see Fig. S7C) (Fei et al., 2007). The pressure difference between the two measured data points was used as the error bar. In addition, we also measured the pressure by using the diamond edge line through the Raman spectroscopy. X-ray scattering patterns of the glass were collected with a Pilatus3X CdTe 300K-W detector, which was calibrated using a LaB6 standard (NIST SRM 660b). We collected data from the empty diamond anvil cell to enable background subtraction. The collection time for each glass X-ray scattering pattern was 600 to 1200s in three different spots in the sample chamber. The opening angle (111.3º) in the horizontal plane allows the Faber-Ziman structure factor S(Q) to reach a maximum of 14 $Å^{-1}$. We used the DIOPTAS software to convert 2D images to 1D angle-

dispersive X-ray scattering patterns and then, employed the Glassure software (Prescher, 2017; Prescher and Prakapenka, 2015) to convert raw data to S(Q) and calculate g(r). Background X-ray scattering from an empty cell was collected at ambient conditions. We used the Glassure software to perform background subtraction, atomic factor corrections, optimization of the scattering data using a Kaplow-type correction (Kaplow et al., 1965) with five iterations. Relaxed glass density from the literature (Petitgirard et al., 2015) was used when analyzing S(Q) and g(r). In addition, the Lorch modification function (Lorch, 1969) was applied to minimize the Fourier transform oscillation (terminal ripples) due to the limited Q range. We also obtained g(r) values without applying Lorch modification function for comparison.

Brillouin spectroscopy measurements

We performed two sets of in-situ Brillouin measurements in a DAC up to 56 GPa. A Coherent Verdi V2 continuous wave solid state laser (laser power: 300 mW; wavelength: 532 nm), a Hamamatsu C11202-050 detector with a typical dark count of 7 cts/sec and a Sandercock-type six-pass tandem Fabry-Perot interferometer were employed to conduct *in-situ* high-pressure Brillouin scattering measurements of $MgSiO_3$ glass in a 50-degree symmetric scattering geometry at room temperature (300 K) (Sinogeikin et al., 2006). The incident laser beam was focused to a ~7 μm beam spot. The abovementioned synthesized $MgSiO_3$ glasses (thin transparent pellet glass for the 1st run and glass powder for our 2nd run) were loaded into the BX-90 diamond anvil cell (DAC) in a glove box in order to prevent contamination of the sample. The cell was equipped with type IA diamond anvils, which had a 0.30-mm culet, and a 10 to 20 μm thick rhenium gasket with a 0.12-mm hole perforated using IR laser drilling device. No pressure medium was used to avoid any scattering effects from the diamond and artificial discontinuities

from the pressure media. A >5 μm spherical ruby and a small piece (10 μm) of Au were placed in the sample chamber for pressure determination. In order to ensure the accuracy of Brillouin scattering data, we measured the pressure before and after acquisition of each spectrum and also collected the FSDP for comparison with our previously obtained X-ray data. The accumulation time for a single measurement ranged from 20 minutes to 2 hours depending on the sample pressure. Compared with ambient data, a longer data collection time was necessary to reach a comparable signal to noise ratio at high pressures. At each pressure point, we collected spectra from three different χ angles (0º, 45º and 90º) and the spectra were analyzed to determine the longitudinal and sheer velocity peak locations by using the Win1024 software.

The density at ambient conditions (2.774 ± 0.014 g/cm^3) was measured from the recovered product of $MgSiO_3$ glass, using the Archimedes method. The value is an average of six independent measurements. The isothermal bulk and shear moduli were calculated from the velocities using the third- and fourth-order Birch-Murnaghan EOS of $MgSiO_3$ with relaxed high-pressure density from the literature (Petitgirard et al., 2015; Sanchez-Valle and Bass, 2010).

SEM analysis

Recovered $MgSiO_3$ glass samples were characterized by a scanning electron microscope (SEM, JEOL JCM-6000Plus) equipped with energy dispersive X-ray spectroscopy (EDXS). Polished $MgSiO_3$ samples were carbon-coated and mounted on a vertical post on the aluminum sample stage. Measurements were conducted with an accelerating voltage of 15 kV and a working distance of 19 mm to determine the sample composition (Fig. S8). Examples of composition analyses are shown in Table S4.

Results

Structural response of $MgSiO_3$ glass to high-pressure by Raman spectroscopy

Samples of $MgSiO_3$ glass were synthesized in the two-step process. We first synthesized pure and anhydrous $MgSiO_3$, hereafter denoted as *ortho*-$MgSiO_3$, which were then melted under 1 GPa pressure and rapidly quenched to ambient temperature (Methods and Figure S1). At ambient conditions, *ortho*-$MgSiO_3$ is characterized by corner-linking SiO_4 chains and belongs to the Pbca space group (D_{2h}) with Z = 8. In total, there are 120 normal vibrational modes, including 117 optical modes ($\Gamma = 30A_g + 30B_g + 29A_u + 28B_u$) and three acoustic modes. Among them, the A_g and B_g modes are Raman active, and A_u and B_u are IR active (Chopelas, 1999). The sharp Raman modes may be divided into three groups. One group, centered around the 300 - 400 cm^{-1} region provides twisting, bending, and stretching vibration of metal oxides. Another around 700 cm^{-1} is due to bending and stretching between adjacent SiO_4 tetrahedra and the other, near 1000 cm^{-1} is due to asymmetric stretching within each individual tetrahedron (Fig. S2A).

In contrast, $MgSiO_3$ glass exhibits much broader Raman peaks in these two frequency regions, owing to the highly disordered nature of the glass (Fig. S2B). The broad peak covering 300 to 800 cm^{-1} can be deconvolved into a minimum of three peaks, two of which, centered at 650 cm^{-1} and 700 cm^{-1}, respectively, are assigned to inter-tetrahedral bending and stretching vibrational modes [denoted as ν_b(Si-O-Si) and ν_s(Si-O-Si)], respectively. A third, much weaker peak centered around 530 cm^{-1}, is assigned to SiO_4 tetrahedra forming 6-, 5-, and 4-membered rings, known as the "defect peak" (Fu et al., 2017; Stolen et al., 1970). The 300 to 500 cm^{-1} region contains information on stretching vibrations of Mg-O_b-Si and O_b-Mg-O_b modes, [where O_b indicates as bridging oxygen] (Kubicki et al., 1992). These modes, however, appear to be

very weak and cannot be confidently observed with Raman. The broad peak covering 800-1200 cm^{-1} is primarily due to vibrational bands of various Q^n species (where n= 0 to 4), which describe the number (n) of interconnected (bridging) oxygen atoms per SiO_4 tetrahedron. The four major Q^n species correspond to SiO_4^{4-} (n=0), $Si_2O_7^{6-}$ (n=1), $Si_2O_6^{4-}$ (n=2), and $Si_3O_5^{2-}$ (n=3) (Kalampounias et al., 2009; Kubicki et al., 1992; McMillan et al., 1992). Deconvolution constrained by Gaussian and Lorentzian functions resolve individual peaks as shown in Fig. S2B. Essentially all Q^n species can be reasonably well distinguished. The fitting shows that Q^2 is the dominant species in $MgSiO_3$ glass, consistent with the 1050 cm^{-1} and 1100 cm^{-1} peaks in *ortho*-$MgSiO_3$ (Fig. S2A), which is a chain silicate with essentially all SiO_4 tetrahedra sharing two oxygen atoms. At ambient pressure, all peak positions of our measurements are in agreement with previous Raman measurements within 5 cm^{-1} (Kubicki et al., 1992; McMillan, 1984; Shim and Catalli, 2009). For Q^4, all four oxygens of a given tetrahedron are bridged with neighboring tetrahedra; the associated antisymmetric stretching vibrations are also likely to be present near 1000-1200 cm^{-1}. These vibrational bands, however, are usually broad and very weak for silicate glasses (McMillan, 1984). Additionally, the species Q^4 overlaps with Q^3 in Raman spectra. In the deconvolution process, we assumed Q^4 to be zero and assigned all the intensity as Q^3, similar to the report by Kalampounias et al. (Kalampounias et al., 2009). This procedure does not significantly affect structural interpretation, as even in NMR studies, the percentage of Q^4 species is low.

We conducted 300 K Raman measurements up to 67 GPa on the $MgSiO_3$ glass. All Raman spectra of $MgSiO_3$ glass presented here are normalized with respect to the boson peak centered at 102 cm^{-1} for ease of comparison. Normalized Raman spectra upon compression and decompression are shown in Figs. 1A and 1B, respectively. Examples of deconvolution for the

290 stretching modes ν_b(Si-O-Si) and ν_s(Si-O-Si) and Q species are shown in Fig. 1C. Raman peak
291 positions are shown in Figure S4A.

292 Upon initial compression, essentially all Raman modes shifted towards high frequencies,
293 except for the defect peak whose intensity decreased continuously (Fig. 2A, Fig. S4A). Above 2
294 GPa, the full width half maximum (FWHM) of the peak representing ν_b(Si-O-Si) and ν_s(Si-O-Si)
295 (~660 cm^{-1}) increased significantly and the peak gradually became asymmetric (Fig. 1C). While
296 ν_b(Si-O-Si) shifted from 664 cm^{-1} (2 GPa) to 687 cm^{-1} (8 GPa) and overlapped more significantly
297 with ν_s(Si-O-Si), a small but noticeable peak (~560 cm^{-1}) emerged at 6 GPa on the left side of
298 ν_b(Si-O-Si). The intensity of this small peak increased with increasing pressure (Fig. 1C) which
299 became prominent at 8 GPa. Also, while the intensities of Q^0 (~888 cm^{-1}) and Q^1 (~940 cm^{-1})
300 decreased with increasing pressure, those of Q^2 (~980 cm^{-1}) and Q^3 (~1060 cm^{-1}) increased,
301 suggesting shifting tetrahedral connections during compression. The defect peak continued to
302 decrease in intensity and completely disappeared at 8 GPa (Figs. 1C and 2A), suggesting
303 diminishing population of the 6-, 5-, and 4-membered tetrahedral rings.

304 Above 8 GPa, a new peak appeared around 600 cm^{-1} (red asterisk next to the 8 GPa spectrum
305 in Fig. 1A). The emergence of this new mode may indicate formation of a new bond in the
306 originally predominantly tetrahedrally coordinated glass structure. This mode is similar to the
307 breathing mode of 3-membered tetrahedral rings at ~605 cm^{-1} observed in amorphous SiO_2 (see
308 Fig. S2C), and can be alternatively assigned to an internal bending mode of O-Si-O (Huang et
309 al., 1999). Thus, we attribute this peak to a structural change from large n-membered rings (n=4,
310 5, 6 etc.) to distorted smaller n-membered rings (n=3 and/or 4) in $MgSiO_3$ glass (Fu et al., 2017;
311 Kohara et al., 2011; Stolen et al., 1970). In addition, it has been suggested that $MgSiO_3$ glass
312 may form oxygen tri-clusters between 12 to 20 GPa (where one oxygen anion is corner-shared

313 by three tetrahedral units) due to the distortion of the tetrahedral network, thereby decreasing
314 O_{nbo} bonding and ∠Si-O-Si angles and increasing the silicon coordination number (Fukui et al.,
315 2017; Lee et al., 2008; Shim and Catalli, 2009). These conclusions are in broad agreement with
316 our findings at 8 GPa.

317 The bending mode ν_b(Si-O-Si) (650 cm^{-1} at ambient pressure) shifted continuously to higher
318 frequencies and merged with the symmetric stretching mode ν_s(O-Si-O) and began to overlap
319 with the broad Q^n species band (800 – 1200 cm^{-1}) at 17.5 GPa (Fig. 1A), suggesting a reduction
320 in both ∠Si-O_b-Si bond angle and Si-O-Si bond length between 8 GPa and 20 GPa. Contrary to
321 ν_b(Si-O-Si), the broad Q^n species band shifted to lower frequencies between ~15.6 GPa and
322 ~17.5 GPa ($\Delta\nu$ = 45 cm^{-1}), due to adjustments of force constants resulting from the formation of
323 additional Si-O bonds in the glass (Nesbitt et al., 2017). Additionally, intensities of Q^0 and Q^3
324 (~883 cm^{-1} and ~1085 cm^{-1} at ambient pressure) gradually diminished from ~8 to ~20 GPa,
325 suggesting that the dominant structural motifs were no longer tetrahedral, but somewhat higher
326 coordinated polyhedral SiO_x (average x>4). Figure S4B summarizes integrated Raman band
327 intensities of various Q species with increasing pressure to ~20 GPa. The Q^0 disappeared at ~8
328 GPa, where the Q^2 reached maximum intensity and began decreasing upon further compression.
329 The intensity of Q^2 became more-or-less constant above 12 GPa. Within their uncertainties, the
330 intensities of Q^1 and Q^3 remained constant until about 14 GPa, where Q^1 began increasing in
331 intensity, while Q^3 decreased rapidly and disappeared at 20 GPa. Such complex evolution
332 indicates that the SiO_4 tetrahedral structural motifs are under continued modification upon
333 compression and that above ~16 GPa, the structure of $MgSiO_3$ glass can no longer be adequately
334 characterized as a tetrahedral network.

After increasing pressure to slightly above 20 GPa, a broad new peak emerged at ~360 cm^{-1} (red asterisk next to the 21.5 GPa spectrum in Fig. 1A). The average Mg coordination number is 4.5 at ambient pressure (Arab et al., 2002). The new peak may signify the formation of higher Mg coordination MgO_y (y>4.5), which, in turn, suggests that Mg^{2+} cations tend to bind with nearest neighboring SiO_x (x>4) structural units. Notably, this Raman mode continuously shifted toward higher frequencies (401 cm^{-1}) with increasing pressure until ~29 GPa, and then rapidly shifted to lower frequencies to 342 cm^{-1} until ~52 GPa. While the stiffening between 21 and 29 GPa may imply strengthening of the SiO_x (x= 5 to 6) bond with decreasing ∠O-Si-O bond angle due to compression, the softening between 29 and 52 GPa may be due to weakening of MgO_y bond before further increase in Mg^{2+} coordination number. The bending mode and the high-frequency broad band continued to broaden from ~34 to 39 GPa, making it difficult to separate individual features. A new band (~860 cm^{-1}) emerged at ~40 GPa, corresponding to octahedrally coordinated SiO_6 and may be directly compared to features in crystalline phases of akimotoite (~22 GPa) and stishovite (~8 GPa), hence providing a hint of SiO and MgO bond lengths in the glass structure (Hemley et al., 1986; Okada et al., 2008). The 860 cm^{-1} band persisted until 67 GPa. Figure 2A summarizes the structural modifications by compression based on Raman mode changes: (i) a discontinuity of Raman peaks at ~900 cm^{-1} and ~512 cm^{-1} at ~8 GPa; (ii) the emergence of a new peak at ~600 cm^{-1} at ~8 GPa; (iii) a discontinuity of the 1096 cm^{-1} peak at ~20 GPa; (iv) the emergence of a new peak at ~360 cm^{-1} at 20 GPa; (v) the emergence of a new peak at 860 cm^{-1} at 40 GPa.

During decompression, the peak at 860 cm^{-1} exhibited substantial hysteresis and persisted until ~29 GPa (Figs. 1B and 2A). It disappeared upon further pressure release, whereas all other peaks remained until ambient pressure was reached. This suggests that the highly coordinated Si

in SiO_x (x>4) was predominant above 30 GPa. In other words, the immediately recovered product was composed primarily of SiO_x (x>4) and MgO_y (y>4.5) at ambient condition. As shown in Fig. S8C, however, such densified $MgSiO_3$ glass can be retained only in a short period of time from 40 minutes to several days, before reverting to its initial structure. The decompressed sample underwent irreversible changes with noticeable cracks in the center. These observations suggest that the strength of the glass was not sufficient to maintain the internal stress caused by densely packed SiO_x (x>4) and MgO_y (y>4.5) configurations. Over time, the structure reverted back to the lower-pressure form, with significant volume expansion, resulting in cracking.

Structural response to pressure, studied by X-ray scattering

Synchrotron angle dispersive X-ray scattering data were collected on $MgSiO_3$ glass up to 72 GPa using a CdTe photon-counting detector with a multi-channel collimator (MCC) (see Methods) (Prescher et al., 2017; Yu et al., 2019). Figure 3A shows selected structure factors, S(Q) at various pressures. The ambient pressure S(Q) exhibits three characteristic peaks below Q = 6 $Å^{-1}$. The first strong diffraction peak (FSDP) at 1.89 $Å^{-1}$, a very weak peak at 3.04 $Å^{-1}$, and a strong and broad peak at 4.56 $Å^{-1}$. Upon compression up to ~9 GPa, the FSDP shifted rapidly to higher Q (Figs. 2B and 3A). The weak peak shifted to lower Q (from 3.04 $Å^{-1}$ to 2.96 $Å^{-1}$) below ~9 GPa, with a slight but rapid increase in intensity (Fig. 3A). Around ~9.8 GPa, the FSDP position exhibited a sudden jump (Fig. 2B) and the original weak peak around 3 $Å^{-1}$ began increasing in intensity rapidly (Fig. 3A). Upon further increase in pressure, the intensity of the third peak increased, but mainly by broadening, while the intensity of FSDP continued to decrease. Overall, the behavior resembles that observed in SiO_2 glass, in which the FSDP exhibits the largest jump around 14 GPa (Prescher et al., 2017). The substantially lower pressure

(~9 GPa) of the FSDP jump in $MgSiO_3$ glass (dominated by Q^2 species forming tetrahedral chains in the presence of MgO_y polyhedral) compared to SiO_2 glass (a three-dimensional tetrahedral network dominated by Q^4 and n-membered rings) is attributed to increased atomic packing density and increased internal pressure, facilitating structural reconfiguration. According to Kohara et al. (2011), the void space in SiO_2 glass takes up ~32% of the total volume, whereas in $MgSiO_3$ glass, the addition of MgO in the glass reduces void space to almost zero (<3%) (Kohara et al., 2011). Thus, upon compression, the additional Mg^{2+} and O^{2-} ions located in interstitial space in the SiO_x tetrahedral network, may counteract the compression by generating internal chemical pressure, thereby enhancing structural stability.

Figure 3B shows the real-space pair distribution function (PDF), g(r), with (black curves) and without (red dotted curves) applying the Lorch function to address effects of the finite Q range (Lorch, 1969). The amplitudes of the ripples in the red dotted curves provide a rough estimate of the uncertainties in g(r) of our experiments. With the application of the Lorch function, ripples due to truncation effects are effectively smoothed out. However, the smoothing made it more difficult to determine Si-O, Mg-O, O-O, and Si-Si bond distances. In this respect, individual bond distances of Si-O (r_{Si-O}), and Si-Si (r_{Si-Si}) were determined using the Gaussian distribution functions to deconvolve the g(r) peaks after applying the Lorch modification function. In addition, as can be seen in Figs. 2C, 2D, and Fig. 5, the bond distances of r_{Si-O}, r_{Mg-O}, r_{O-O}, and r_{Si-Si} obtained from results without applying the Lorch function can also help to locate the peak positions of g(r) (Niida et al., 2001); however, in this case, we cannot completely rule out the possibility that some of the peaks may be affected by the ripples. Thus, it appears to be important to compare the bond distances with those obtained from applying the Lorch modification function (Table S2). With this caveat in mind, we examine these distances as a function of

404 pressure and compare our results of r_{Si-O}, r_{MgO}, r_{O-O}, and r_{Si-Si} with previous studies (Figs. 5, S5,
405 and Table 2). Bond angles ∠Si-O-Si and ∠O-Si-O were then determined using the simple sine
406 rule.

407 At ambient condition, our results yield r_{Si-O} = 1.622 (±0.008) Å, r_{Mg-O} = 2.034 (±0.015) Å, r_{O-}
408 $_{O}$ = 2.633 (±0.015) Å and r_{Si-Si} = 3.098 (±0.008) Å with applying the Lorch modification
409 function, whereas without applying the Lorch modification function yields r_{Si-O} = 1.602 (±0.020)
410 Å, r_{Mg-O} = 2.051 (±0.030) Å, r_{O-O} = 2.575 (±0.030) Å and r_{Si-Si} = 3.056 (±0.016) Å with larger
411 amplitude differences, most of which are in line with previous MD simulations and experimental
412 studies (Ghosh et al., 2014; Kono et al., 2018; Salmon et al., 2019). The ambient Si-Si distance
413 reported in Kono et al. was based on data collected over a greater Q range than the rest of their
414 high-pressure data. The agreement between our data and that of Kono et al. between 10 and 20
415 GPa, suggests that their ambient data may have different systematic errors than the high-pressure
416 results. The observed average r_{Si-O} and r_{Mg-O} increase with pressure until 9.8 (±2.0) GPa (Figs. 2C
417 and S5A). On the other hand, both r_{Si-Si} and r_{O-O} decrease with pressure (Figs. 2D, S5B-C and
418 Table S2), suggesting increasing distortion in the tetrahedral SiO_4 network, which can lead to a
419 decrease in Si-O-Si bond angles and ring size distributions with permanent densification (Huang
420 and Kieffer, 2004).

421 Above ~9 GPa, the increase in r_{Si-O} accelerates (Figs. 2C and S5A), while r_{O-O} and r_{Si-Si}
422 decrease continuously (Fig. 2D and S5C). Both ∠Si-O-Si and ∠O-Si-O decreased gradually from
423 ~145.1º and ~107.0º at ambient pressure to ~118.5º and ~93.7º, respectively, at ~20 GPa (Fig.
424 2E). The ∠Si-O-Si angles may be interpreted as network distortion and the ∠O-Si-O angle
425 reflects variation within the polyhedral motifs from tetrahedral SiO_4 to highly coordinated SiO_x
426 ($4 \leq x \leq 5$). On the other hand, the large increase in r_{Si-O}, between 8 and 20 GPa (Fig. 2C) is viewed

This is the peer-reviewed, final accepted version for American Mineralogist, published by the Mineralogical Society of America.
The published version is subject to change. Cite as Authors (Year) Title. American Mineralogist, in press.
DOI: https://doi.org/10.2138/am-2022-7969. http://www.minsocam.org/

as evidence for the occurrence higher coordinated SiO_x ($5 \leq x \leq 6$) and MgO_y (y increased from ~4.5 at ambient condition to $4.5 \leq y \leq 8$). Tri-cluster oxygens have been reported in this pressure range (Lee et al., 2008). Such tri-clusters would be accompanied by the formation of pseudo penta-coordinated $Si\text{-}O_x$ structural motifs. Our observed bond angles show a close resemblance to the bond angles in a trigonal bipyramidal arrangement, in agreement with the conclusion of Lee et al.

Between ~20 and 40 GPa, $r_{Mg\text{-}O}$, $r_{O\text{-}O}$, and $r_{Si\text{-}Si}$ all decreased continuously (Fig. 2D, Fig. S5). $r_{Si\text{-}O}$, on the other hand, increased very slightly. Within this pressure range, both bond distance and angles suggest that $MgSiO_3$ glass gradually underwent a structural modification by forming an edge-sharing octahedral network, similar to crystalline $MgSiO_3$ akimotoite ($r_{Si\text{-}O}$: ~1.768 Å; ∠O-Si-O: ~86.1º at 0 GPa) (Horiuchi et al., 1987; Karki et al., 2000).

Above 40 GPa, $r_{Si\text{-}O}$, $r_{O\text{-}O}$, and $r_{Si\text{-}Si}$ decreased gradually with pressure while the bond angles remained roughly constant, reflecting normal compression behavior in octahedrally coordinated glass. In contrast, rMgO overlaps with Si-O peak above ~30 GPa, thus accurately measuring rMgO is challenging and cannot be determined. However, the bond distance of MgO is expected to increase with increasing pressure ranged between ~30 and ~52 GPa since the Raman frequency shifts negatively from 401 cm^{-1} at ~29 GPa to 342 cm^{-1} at ~52 GPa (Δ=59 cm^{-1}), implying that the rMgO bond is weakened.

Elastic responses of $MgSiO_3$ glass to pressure, studied by Brillouin spectroscopy

Figure 2F summarizes longitudinal (V_p) and shear (V_s) wave velocities of $MgSiO_3$ glass up to 56 GPa. Data from two high-pressure experiments gave consistent and reproducible results, which, in turn, show excellent correlation with our X-ray scattering and Raman data. Overall, our

449 results are consistent with previous MD calculations and experiments (Ghosh et al., 2014;
450 Murakami and Bass, 2011; Sanchez-Valle and Bass, 2010).

451 Between 0 and 2 GPa, there is significant stiffening in both V_p and V_s, resulting in a dramatic
452 increase in bulk and shear moduli as well as Poisson's ratio (Fig. S6C-D). This change in
453 elasticity correlates with the increase in FWHM of the Raman bending mode around 660 cm^{-1}
454 and the disappearance of the defect mode around ~538 cm^{-1} representing the 6-, 5-, 4-membered
455 rings (Fu et al., 2017; Kohara et al., 2011; Stolen et al., 1970). From ~2 to ~8 GPa velocities
456 increase nearly linearly at significantly slower rates (Fig. 2F).

457 The change in pressure dependence at 8 GPa corresponds very well to the disappearance of
458 the Q modes (Q^0 or Q^1), the disappearance of the 6- and 5-membered rings (Fig. 2A), and the
459 marked discontinuity in the FSDP in Raman spectra (Fig. 2B). The pressure dependence of V_p
460 and V_s above 8 GPa also increased significantly compared to that below 8 GPa. The kink in V_p
461 near 20 GPa corresponds to the disappearance of Q^3 mode and the emergence of the new broad
462 Raman band at 359 cm^{-1} (Fig. 2A), the drastic change in the Si-O distance versus pressure curve
463 (Fig. 2C), and the change in pressure dependence of the bond angles from g(r) (Fig. 2E). All of
464 these suggest the development of higher Si and Mg coordination in SiO_x and MgO_y polyhedra. A
465 decrease in pressure dependence occurred in both V_p and V_s near ~15 GPa, corresponding to the
466 pressure dependence in the r_{Si-O} distance (Fig. 2C). The next change in pressure dependence in
467 V_p and V_s occurred at 20 GPa, where both r_{Si-O} distance and bond angles exhibited large changes.
468 Above 20 GPa, pressure dependence remained essentially constant until 40 GPa. Further
469 compression to 56 GPa, V_p and V_s progressively increased with pressure, with somewhat lower
470 pressure dependence than that below 40 GPa. These observations are consistent with the Raman

and X-ray results (Fig 2A-2E), which indicate a continuous structural evolution in response to pressure towards a 5-fold to 6-fold coordinated network.

Figure S6B and Table S3 compare our results with previous Brillouin spectroscopy data (20, 21). Two important distinctions should be noted: (i) our V_p and Vs (V_p: ~7.3 km/s and V_s: ~3.9 km/s between ~2 and 8 GPa) are higher than that of Sanchez-Valle and Bass, 2010 (V_p: ~7.0 km/s and V_s: ~3.7 km/s); (ii) in the pressure ranges from ~14 to ~56 GPa, our V_p and V_s values are considerably lower (~5% to ~9%) than those of Murakami and Bass, 2011 and Sanchez-Valle and Bass, 2010. Such different responses of elastic velocities may be attributed to different concentrations of SiO_2:MgO (Sanchez et al., 2009, (61.1:38.6 wt.%); This study (49:51 wt.%)), and pressure media (Methanol-Ethanol-Water; Argon gas) used in the different studies. Therefore, only our own Brillouin data can be directly compared with the Raman and XRD data in Fig. 2, as all have the same composition and pressure environment.

Discussion and implications

Correlation between structural evolution and elastic properties

We have developed a model for structural evolution of $MgSiO_3$ glass by combining Raman and X-ray scattering observations, which, in turn, is supported by elastic property changes determined by Brillouin light scattering. At ambient condition, Table 1 compares our Q^n (n = 0, 1, 2, 3, 4) speciation of $MgSiO_3$ glass with those at 1 bar from previous experiments and MD calculations (Davis et al., 2011; Ghosh et al., 2014; Kalampounias et al., 2009; Kubicki and Lasaga, 1991; Salmon et al., 2019; Sen et al., 2009). It is interesting to note that the Raman result tends to give high estimations on Q^0, whereas NMR spectra tends to give low estimations, with

MD results vary widely from nearly 0 (4%) to 20%. This is primarily due to the fact that Q^0 species percentage is low and overlapped with Q^1 species. On the other hand, experimental and MD calculated values of Q^1, Q^2, and Q^3 are in broad agreement. Additionally, the Q^2 species is more abundant than Q^0, Q^1, Q^3 among all the Q species at ambient conditions, suggesting that the $MgSiO_3$ glass is predominantly composed of both tetrahedral chains and n-membered rings (n = 6, 5, 4; conceptually illustrated by Fig. 4A). With pressure increasing to 2 GPa, the defect Raman band at 470 cm^{-1} (Fig. 1C) shows a decrease in the intensity and broadening of the peak. This implies that reductions in the large n-membered rings generate more chain interconnectivity between adjacent molecules which lead to the formation of chain folding and/or become a part of n-membered rings (Fig. 4B). Within this narrow pressure range, sound velocities increase rapidly (Fig. 2F), which is interpreted as being due to reduced void space in the glass due to the distortions. X-ray scattering, which provide spatially and volumetrically averaged atomic arrangement, does not show noticeable changes.

Above 2 GPa, concentrations of Q^1 and Q^2 species increase (Figs. 4B and S4B), as individual monomers (SiO_4^{4-}) bind to form dimers ($Si_2O_7^{6-}$) as well as through reactions such as $Q^0 + Q^3 \rightarrow 2Q^2$ (Fig. 4B). Meanwhile, larger n-membered rings are continuously reduced in size to become 4- and/or 3-membered. X-ray data show that r_{Si-O} increases slightly, while r_{Si-Si} decreased. Both inter- and intra-tetrahedral angles decrease slightly. These structural changes have little effect on sound velocities, which remain more-or-less constant as pressure increases from 2 to 8 GPa. By 8 GPa, oxygen tri-clusters begin to form (Fig. 4C) when large n-membered rings are reduced to 4- or 3-membered rings, introducing drastic changes in medium-range ordering (MRO), resulting in the disappearance of defect Raman peaks, the appearance of a new peak near ~600 cm^{-1} (Figs. 1A, 1C, and 2A), and a large discontinuity in FSDP in S(Q) (Fig. 2B). In other words, upon

compression, the local structural distortion evolves by reducing the average size of n -membered rings. In doing so, tetrahedral chains are bent so that individual tetrahedra approach each other forming oxygen tri-clusters. This effect may be the cause of the appearance of the Raman peak around 600 cm^{-1} (4-, 3-membered ring) and corresponding changes in the bond distance and angles.

Between 8 GPa and 20 GPa, pressure-induced distortion occurs within 4-, 3-membered rings, forming pseudo penta-coordinated Si-O polyhedral. With increasing Si coordination, the average Si-O bond distance increases rapidly (Fig. 2C). The ∠O-Si-O angle decreases from the nearly ideal tetrahedral value (109.5°) towards octahedral (90°) angles (Fig. 2E). The ∠Si-O-Si angle follows suit. The ~600 cm^{-1} Raman peak continues to broaden with increasing intensity from 8 to 20 GPa and moves toward lower wavenumbers, suggesting changes in Si-O interaction. The pressure dependence of the Q^2 position near 1000 cm^{-1} changes abruptly from positive to negative near 16 GPa (Fig. 2A) and the global distribution of other Q species also changes around the same pressure (Fig. S4B) due to the increase in Si coordination. Additionally, the presence of highly coordinated SiO_x (x= 5, 6) polymorphs can also be identified by the peak broadening on the right side of the ν_b(Si-O-Si) mode around 750 cm^{-1} at 17.5 GPa. The existence and position of an overlapped peak can be found by deconvolution (Fig. S4C). The intensity of this peak increases with pressure and becomes prominent at ~40 GPa. This overlapped band at ~750 cm^{-1} (17.5 GPa) and the well-resolved peak at ~ 860 cm^{-1} (40 GPa) show good agreement with the earlier literature values of the A_{1g} mode of crystalline stishovite at 1 bar and 40 GPa, respectively (Kingma et al., 1995). Correspondingly, the r_{Si-O} distance increases more rapidly (Fig. 2C), and the longitudinal velocity exhibits a change in slope near 16 GPa (Fig. 2F), in good agreement with MD simulation studies (black dashed curve) (Ghosh et al., 2014).

539 Above 20 GPa, $MgSiO_3$ glass can no longer be characterized as tetrahedrally coordinated, as
540 fractions of SiO_5 and SiO_6 species increase with pressure (Fig. 4E). The ~1000 cm^{-1} Raman peak
541 that changed to near 950 cm^{-1} may reflect increased fractions of SiO_6 species (Fig. 2A). The Si-O
542 distance remains more-or-less constant up to 40 GPa (Fig. 2C) and the ∠O-Si-O and ∠Si-O-Si
543 angles decrease monotonically (Fig. 2E). Sound velocities increase slightly faster with pressure
544 than in the pressure range between 8 and 20 GPa due to increased fractions of SiO_6 species.

545 Above 40 GPa, essentially all Si atoms have become octahedrally coordinated (Fig. 4F). Si-O
546 and Si-Si distances decrease slightly with pressure (Fig. 2C), which is a normal compression
547 response. Bond angles remain more or less constant with pressure (Figs. 2D and 2E). Sound
548 velocities continue to increase with pressure, albeit at a slower rate.

549 There are some disparities in elastic responses between our data and previous studies. The
550 different pressure media used in Sanchez-Valle and Bass (2010), could not provide hydrostatic
551 condition throughout the pressure range in their study. For instance, the methanol-ethanol-water
552 (16:3:1 ratio) mixture, solidifies at about 9 GPa. As a result, nonhydrostatic stress in such a
553 pressure medium increases rapidly from 0 to 3 GPa at pressures of 20 - 23 GPa (Klotz et al.,
554 2009). For Ar gas, nonhydrostatic stress increases from 0 GPa at zero pressure to about 0.2 GPa
555 at around 18 GPa. After 18 GPa, non-hydrostatic stress accelerates and then becomes ~1.2 GPa
556 at 40 GPa. These changes in non-hydrostatic stress are likely to introduce artificial
557 discontinuities or slope changes in Raman peaks and Brillouin velocities. As can be seen in Fig.
558 S6B, both compressional (V_p) and shear (V_s) velocities in Sanchez-Valle and Bass (2010) (dark
559 grey dots) show a sudden increase after around 18 GPa, which may be attributed to Ar
560 solidification. Also, their first kink in velocities occurs at 8 GPa, which is not far from the
561 solidification pressure of 9 GPa in methanol-ethanol-water. According to Klotz et al. (2009),

helium (He) pressure media can ensure good approximation and constant-pressure conditions; however, Shen et al. (2011) recently reported that the He atoms tend to enter the structure of SiO_2 glass, making much less compressible (Klotz et al., 2009; Shen et al., 2011). Therefore, further studies are needed to clarify the effects of pressure-media on the elastic properties of the various glasses.

Effects of MgO on Structural and Physical Properties of MgO-SiO_2 Glasses and Melts

To gain insights into the role of Mg-O in affecting compression behavior in silicate glasses, we next examine reported structural and physical property data on SiO_2, $MgSiO_3$, and Mg_2SiO_4 glasses [Table 2. (Benmore et al., 2011; Cormier and Cuello, 2011; Kohara et al., 2011; Kohara et al., 2004; Kono et al., 2011; Lesher et al., 2009; Petitgirard et al., 2015; Yokoyama et al., 2010)] and compare our pressure dependent Si-O and Mg-O bond lengths with those reported in previous experimental studies (Benmore et al., 2011; Prescher et al., 2017) and MD simulations (Kohara et al., 2011; Kohara et al., 2004). At ambient pressure, the structure of SiO_2 glass is characterized by a three-dimensional (3D) network in which essentially all tetrahedra are linked to adjacent tetrahedra at four corners. MD simulations show that roughly 32% of the network volume is occupied by cavities (Kohara et al., 2011). When MgO is added to this network to form $MgSiO_3$ and Mg_2SiO_4 glasses, cavity volume is drastically reduced to 3% and 0%, respectively and the average Mg-O coordination numbers in $MgSiO_3$ and Mg_2SiO_4 glasses are 4.5 and 5, respectively (Kohara et al., 2011; Kohara et al., 2004).

Figure 5 shows the complex effect of adding Mg-O molecules to SiO_2 to form $MgSiO_3$ and Mg_2SiO_4 glasses. Although all Si-O lengths start at approximately the same value at zero

584 pressure, with increasing pressure, the Si-O bonds lengthen in SiO_2 and $MgSiO_3$ glasses rapidly,
585 while those in Mg_2SiO_4 glass remain more-or-less constant until ~20 GPa and then begins to
586 increase ever so slightly. It has been shown that an increase in Si-O coordination number is
587 accompanied by the elongation of Si-O bond lengths during compression (Benmore et al., 2010;
588 Meade et al., 1992; Petitgirard, 2017). Indeed, in SiO_2 and $MgSiO_3$ glasses, Si becomes
589 predominantly octahedrally coordinated at pressures above ~25 GPa (Kono et al., 2018; Prescher
590 et al., 2017). For Mg_2SiO_4 glass, the more-or-less constant Si-O bond length up to 30 GPa
591 suggests that the relatively more isolated SiO_4 tetrahedra in this glass are more reluctant to adopt
592 octahedral coordination and that compression up to 30 GPa is predominantly accommodated by
593 the metal oxide (MO) polyhedra. Therefore, much higher pressure is required to achieve higher
594 Si coordination.

595 Mg-O bond length in $MgSiO_3$ and Mg_2SiO_4 glasses also responds to pressure differently (Fig.
596 5B). In $MgSiO_3$ glass, the average Mg-O bond length is more-or-less constant with pressure up
597 to ~10 GPa (from 2.051(30) at 0 GPa to 2.062(30) at 9.8 GPa) and then turns downward with
598 further pressure increases. The decrease in average $r_{Mg\text{-}O}$ may be due to the change in the average
599 Mg-O polyhedral shape. The subsequent decrease in bond length is more-or-less a normal
600 compression behavior until ~30 GPa. However, as pressure increases to above 30 GPa, it
601 becomes more difficult to determine Mg-O distance, as severe peak overlap occurs (Fig. 3B).

602 In Mg_2SiO_4 glass, Mg-O bond length decreases linearly from 2.02 Å at 1 bar to 1.92 Å at 30
603 GPa, whereas average Mg-O coordination number increases monotonically from 5 to about 6.6
604 (Benmore et al., 2011). There is also evidence that Mg-O polyhedra are highly distorted with
605 mixed 4-, 5-, and 6-fold coordination with oxygen (Kohara et al., 2004). With a molar ratio of
606 $MgO/SiO_2=2$, the structure of Mg_2SiO_4 glass is characterized by isolated SiO_4 tetrahedra

607 (NBO/T=0) embedded in a corner- and edge-sharing Mg-O polyhedral network, which largely
608 controls the compression behavior of this glass. This is in sharp contrast to the structure of
609 $MgSiO_3$ glass, in which each SiO_4 tetrahedron typically shares two corners with adjacent
610 tetrahedra (NBO/T=2), which may be considered the load-bearing framework. Indeed, between
611 10 and 30 GPa, the average Mg-O distances in $MgSiO_3$ and Mg_2SiO_4 glasses follow roughly the
612 same trend, with $r_{(Mg-O)}$ in $MgSiO_3$ glass somewhat larger, suggesting that at the same pressure
613 Mg-O polyhedra in Mg_2SiO_4 glass are under more compression.

614 Different structural characteristics result in distinct physical properties. Ambient density
615 increases with increasing MgO concentration, reflecting diminishing cavities with increasing
616 MgO concentration (Table 2). Zero-pressure isothermal bulk modulus (K_{T0}), on the other hand,
617 exhibits a complex relationship with MgO concentration, with that of $MgSiO_3$ glass being the
618 lowest among the three compositions. Even more complex is the pressure derivative of bulk
619 modulus (K'_{T0}). For SiO_2 glass, the initial K'_{T0} is negative, due to the largely open but fully
620 connected and stiff SiO_4 tetrahedral network, which buckles under initial compression (Wang et
621 al., 2014), reducing rigidity; K_{T0} reaches the minimum around 3 GPa and then begins increasing
622 (Kono et al., 2011). For $MgSiO_3$ glass, K_{T0} is much lower than both SiO_2 and Mg_2SiO_4 glasses
623 but has a very high K'_{T0}. Such a combination may be due to the low cavity concentration but
624 weaker Mg-O bonding (longer Mg-O bond distance than in Mg_2SiO_4 glass) in this glass. The
625 initial compression (K_{T0}) is dominated by the response of Mg-O polyhedra, which, at >15 GPa,
626 help transmit pressure onto the SiO_4 tetrahedra, causing the Si-O coordination number to
627 increase at a similar rate to that in SiO_2 glass, with significantly increased rigidity. For Mg_2SiO_4
628 glass the structure is fully packed so that its K_{T0} is approaching that of the crystalline counterpart
629 forsterite (Suzuki et al., 1983). Its low K'_{T0} (much lower than its crystalline counterpart) may be

due to the accommodating effects of more compressible Mg-O polyhedra, which also delay the increase in Si-O coordination number.

Our multi-faceted experimental and analytical approach demonstrates an effective method to identify and isolate the controlling factors in structural evolution of silicate glasses under high pressure. The significance of this study can be summarized in the following areas:

- our combined dataset provides consistent and complementary evidence of a series of structural modifications in $MgSiO_3$ glass at ~2, ~8, ~20, and ~40 GPa,
- a model describing essentially all the details of structural evolution with pressure, with associate elastic responses of the glass, and
- our data compared with Mg_2SiO_4 glass allow discussion on how composition (especially MgO) affects the compression behavior of silicate supercooled liquids along the MgO-SiO_2 join.

A complete understanding of the structural modification in silicate glasses at ultrahigh pressure requires further clarification by studying systematic patterns, aided by theoretical simulation. With improved experimental capabilities and theoretical simulations, experimental data based on the multi-faceted approach may enable better prediction of silicate liquid structure, reaction mechanism and density under deep mantle conditions.

Acknowledgements

The work was performed at the University of Chicago Center for Advanced Radiation Source (CARS), Advanced Photon Source Sector (APS) 13 IDC/D and 13 BMD Argonne National Laboratory (ANL), and supported by the National Science Foundation-Earth Science (EAR-

652 1620548), Department of Energy Geosciences (DOE) contract No. DE-FG020-94ER14466,
653 DOE Advanced Photon Source (APS), Argonne National Laboratory contract No. DE-AC02-
654 06CH11357. Y-J. R is sincerely thankful to Professors Y. Kono (Ehime Univ., Japan), C-S. Yoo
655 (Washington State Univ., USA), S-H. Shim. (Arizona State Univ., USA) and Drs. N.
656 Velisavjevic, M. Somayazulu, G. Shen, C. Park, and C. K. Benson (High Pressure Collaborative
657 Access Team, sector 16, APS, ANL, USA) for their insightful discussions; Drs. T. Officer, F.
658 Shi, and S. Chariton for their assistance; and M. Proskey, G. Macha, M. Spears (CARS) for their
659 excellent technical support.

660

661 **Supplementary material**

662 Supplementary information is available in the online version of the paper. Correspondence
663 and requests for materials should be addressed to Y-J. R (ryu@cars.uchicago.edu).

664

665 **REFERENCES**

666

667 Agee, C.B., and Walker, D. (1988) Static compression and olivine flotation in ultrabasic silicate
668 liquid. Journal of Geophysical Research, 93(B4).
669 Akahama, Y., and Kawamura, H. (2006) Pressure calibration of diamond anvil Raman gauge to
670 310 GPa. Journal of Applied Physics, 100(4), 043516.
671 Arab, M., Bougeard, D., and Smirnov, K.S. (2002) Experimental and computer simulation study
672 of the vibrational spectra of vermiculite. Physical Chemistry Chemical Physics, 4(10),
673 1957-1963.
674 Badro, J., Brodholt, J.P., Piet, H., Siebert, J., and Ryerson, F. (2015) Core formation and core
675 composition from coupled geochemical and geophysical constraints. Proceedings of the
676 National Academy of Sciences, 112(40), 12310-12314.
677 Benmore, C.J., Soignard, E., Amin, S.A., Guthrie, M., Shastri, S.D., Lee, P.L., and Yarger, J.L.
678 (2010) Structural and topological changes in silica glass at pressure. Physical Review B,
679 81(5), 054105.
680 Benmore, C.J., Soignard, E., Guthrie, M., Amin, S.A., Weber, J.K.R., McKiernan, K., Wilding,
681 M.C., and Yarger, J.L. (2011) High pressure X-ray diffraction measurements on Mg_2SiO_4
682 glass. Journal of Non-Crystalline Solids, 357(14), 2632-2636.

683 Boyet, M., and Carlson, R.W. (2005) ^{142}Nd evidence for early (> 4.53 Ga) global differentiation
684 of the silicate Earth. Science, 309(5734), 576-581.
685 Chopelas, A. (1999) Estimates of mantle relevant Clapeyron slopes in the $MgSiO_3$ system from
686 high-pressure spectroscopic data. American Mineralogist, 84(3), 233-244.
687 Cormier, L., and Cuello, G.J. (2011) Mg coordination in a $MgSiO_3$ glass using neutron
688 diffraction coupled with isotopic substitution. Physical Review B, 83(22), 224204.
689 Davis, M.C., Sanders, K.J., Grandinetti, P.J., Gaudio, S.J., and Sen, S. (2011) Structural
690 investigations of magnesium silicate glasses by 29Si 2D Magic-Angle Flipping NMR.
691 Journal of Non-Crystalline Solids, 357(15), 2787-2795.
692 Dewaele, A., Torrent, M., Loubeyre, P., and Mezouar, M. (2008) Compression curves of
693 transition metals in the Mbar range: Experiments and projector augmented-wave
694 calculations. Physical Review B, 78(10), 104102.
695 Fei, Y., Ricolleau, A., Frank, M., Mibe, K., Shen, G., and Prakapenka, V. (2007) Toward an
696 internally consistent pressure scale. Proceedings of the National Academy of Sciences,
697 104(22), 9182-9186.
698 Fu, X., Wang, A., and Krawczynski, M.J. (2017) Characterizing amorphous silicates in
699 extraterrestrial materials: Polymerization effects on Raman and mid-IR spectral features of
700 alkali and alkali earth silicate glasses. 122(5), 839-855.
701 Fukui, H., Hiraoka, N.J.P., and Minerals, C.o. (2017) Electronic and local atomistic structure of
702 MgSiO3 glass under pressure: a study of X-ray Raman scattering at the silicon and
703 magnesium L-edges. 45, 211-218.
704 Ghosh, D.B., Karki, B.B., and Stixrude, L. (2014) First-principles molecular dynamics
705 simulations of $MgSiO_3$ glass: Structure, density, and elasticity at high pressure. American
706 Mineralogist, 99(7), 1304-1314.
707 Hemley, R.J., Mao, H.K., and Chao, E.C.T. (1986) Raman spectrum of natural and synthetic
708 stishovite. Physics and Chemistry of Minerals, 13(5), 285-290.
709 Holtgrewe, N., Greenberg, E., Prescher, C., Prakapenka, V.B., and Goncharov, A.F. (2019)
710 Advanced integrated optical spectroscopy system for diamond anvil cell studies at
711 GSECARS. High Pressure Research, 39(3), 457-470.
712 Horiuchi, H., Ito, E., and Weidner, D.J. (1987) Perovskite-type $MgSiO_3$; single-crystal X-ray
713 diffraction study. American Mineralogist, 72(3-4), 357-360.
714 Huang, L., and Kieffer, J. (2004) Amorphous-amorphous transitions in silica glass. I. Reversible
715 transitions and thermomechanical anomalies. Physical Review B, 69(22), 224203.
716 Huang, Y., Jiang, Z., and Schwieger, W. (1999) Vibrational spectroscopic studies of layered
717 silicates. Chemistry of Materials, 11(5), 1210-1217.
718 Kalampounias, A.G., Nasikas, N.K., and Papatheodorou, G.N. (2009) Glass formation and
719 structure in the $MgSiO_3$–Mg_2SiO_4 pseudobinary system: From degraded networks to
720 ioniclike glasses. Journal of Chemical Physics, 131(11), 114513.
721 Kaplow, R., Strong, S.L., and Averbach, B.L. (1965) Radial Density Functions for Liquid
722 Mercury and Lead. Physical Review, 138(5A), A1336-A1345.
723 Karki, B.B. (2010) First-principles molecular dynamics simulations of silicate melts: structural
724 and dynamical properties. Reviews in Mineralogy and Geochemistry, 71(1), 355-389.
725 Karki, B.B., Duan, W., Da Silva, C.R.S., and Wentzcovitch, R.M. (2000) Ab initio structure of
726 $MgSiO_3$ ilmenite at high pressure. American Mineralogist, 85(2), 317-320.
727 Kingma, K.J., Cohen, R.E., Hemley, R.J., and Mao, H.-k. (1995) Transformation of stishovite to
728 a denser phase at lower-mantle pressures. Nature, 374(6519), 243-245.

729 Klotz, S., Chervin, J.C., Munsch, P., and Le Marchand, G. (2009) Hydrostatic limits of 11
730 pressure transmitting media. Journal of Physics D: Applied Physics, 42(7), 075413.
731 Kohara, S., Akola, J., Morita, H., Suzuya, K., Weber, J.K.R., Wilding, M.C., and Benmore, C.J.
732 (2011) Relationship between topological order and glass forming ability in densely packed
733 enstatite and forsterite composition glasses. Proceedings of the National Academy of
734 Sciences, 108(36), 14780-14785.
735 Kohara, S., Suzuya, K., Takeuchi, K., Loong, C.-K., Grimsditch, M., Weber, J.K.R., Tangeman,
736 J.A., and Key, T.S. (2004) Glass Formation at the Limit of Insufficient Network Formers.
737 Science, 303(5664), 1649-1652.
738 Kono, Y., Shibazaki, Y., Kenney-Benson, C., Wang, Y., and Shen, G. (2018) Pressure-induced
739 structural change in $MgSiO_3$ glass at pressures near the Earth's core–mantle boundary.
740 Proceedings of the National Academy of Sciences, 115(8), 1742-1747.
741 Kono, Y., Yamada, A., Wang, Y., Yu, T., and Inoue, T. (2011) Combined ultrasonic elastic wave
742 velocity and microtomography measurements at high pressures. Review of Scientific
743 Instruments, 82(2), 023906.
744 Kubicki, J., and Lasaga, A.C. (1988) Molecular dynamics simulations of SiO_2 melt and glass;
745 ionic and covalent models. American Mineralogist, 73(9-10), 941-955.
746 Kubicki, J.D., Hemley, R.J., and Hofmeister, A.M. (1992) Raman and infrared study of pressure-
747 induced structural changes in $MgSiO_3$, $CaMgSi_2O_6$, and $CaSiO_3$ glasses. American
748 Mineralogist, 77(3-4), 258-269.
749 Kubicki, J.D., and Lasaga, A.C. (1991) Molecular dynamics simulations of pressure and
750 temperature effects on MgSiO3 and Mg2SiO4 melts and glasses. Physics and Chemistry of
751 Minerals, 17(8), 661-673.
752 Labrosse, S., Hernlund, J.W., and Coltice, N. (2007) A crystallizing dense magma ocean at the
753 base of the Earth's mantle. Nature, 450(7171), 866-869.
754 Lee, S.K., Lin, J.-F., Cai, Y.Q., Hiraoka, N., Eng, P.J., Okuchi, T., Mao, H.-k., Meng, Y., Hu,
755 M.Y., and Chow, P. (2008) X-ray Raman scattering study of $MgSiO_3$ glass at high pressure:
756 Implication for triclustered $MgSiO_3$ melt in Earth's mantle. Proceedings of the National
757 Academy of Sciences, 105(23), 7925-7929.
758 Lesher, C.E., Wang, Y., Gaudio, S., Clark, A., Nishiyama, N., and Rivers, M. (2009) Volumetric
759 properties of magnesium silicate glasses and supercooled liquid at high pressure by X-ray
760 microtomography. Physics of the Earth and Planetary Interiors, 174(1), 292-301.
761 Li, J., and Agee, C.B. (1996) Geochemistry of mantle–core differentiation at high pressure.
762 Nature, 381(6584), 686-689.
763 Lorch, E. (1969) Neutron diffraction by germania, silica and radiation-damaged silica glasses.
764 Journal of Physics C: Solid State Physics, 2(2), 229.
765 McMillan, P. (1984) Structural studies of silicate glasses and melts-applications and limitations
766 of Raman spectroscopy. american Mineralogist, 69(7-8), 622-644.
767 McMillan, P.F., Wolf, G.H., and Poe, B.T. (1992) Vibrational spectroscopy of silicate liquids
768 and glasses. Chemical Geology, 96(3-4), 351-366.
769 Meade, C., Hemley, R.J., and Mao, H.K. (1992) High-pressure x-ray diffraction of SiO_2 glass.
770 Physical Review Letters, 69(9), 1387-1390.
771 Meade, C., and Jeanloz, R. (1988) Effect of a coordination change on the strength of amorphous
772 SiO_2. Science, 241(4869), 1072-1074.

Murakami, M., and Bass, J.D. (2011) Evidence of denser $MgSiO_3$ glass above 133 gigapascal (GPa) and implications for remnants of ultradense silicate melt from a deep magma ocean. Proceedings of the National Academy of Sciences, 108(42), 17286-17289.

Nesbitt, H.W., Henderson, G.S., Bancroft, G.M., and O'Shaughnessy, C. (2017) Electron densities over Si and O atoms of tetrahedra and their impact on Raman stretching frequencies and Si-NBO force constants. Chemical Geology, 461, 65-74.

Niida, H., Uchino, T., Jin, J., Kim, S.-H., Fukunaga, T., and Yoko, T. (2001) Structure of alkali tellurite glasses from neutron diffraction and molecular orbital calculations. 114(1), 459-467.

Ohtani, E. (1988) Chemical stratification of the mantle formed by melting in the early stage of the terrestrial evolution. Tectonophysics, 154(3-4), 201-210.

Okada, T., Narita, T., Nagai, T., and Yamanaka, T. (2008) Comparative Raman spectroscopic study on ilmenite-type $MgSiO_3$ (akimotoite), $MgGeO_3$, and $MgTiO_3$ (geikielite) at high temperatures and high pressures. American Mineralogist, 93(1), 39-47.

Petitgirard, S. (2017) Density and structural changes of silicate glasses under high pressure. High Pressure Research, 37(2), 200-213.

Petitgirard, S., Malfait, W.J., Sinmyo, R., Kupenko, I., Hennet, L., Harries, D., Dane, T., Burghammer, M., and Rubie, D.C. (2015) Fate of $MgSiO_3$ melts at core–mantle boundary conditions. Proceedings of the National Academy of Sciences, 112(46), 14186-14190.

Prescher, C. (2017) Glassure: An API and GUI program for analyzing angular dispersive total X-ray diffraction data. Journal of Zenodo, 10.

Prescher, C., and Prakapenka, V.B. (2015) DIOPTAS: a program for reduction of two-dimensional X-ray diffraction data and data exploration. High Pressure Research, 35(3), 223-230.

Prescher, C., Prakapenka, V.B., Stefanski, J., Jahn, S., Skinner, L.B., and Wang, Y. (2017) Beyond sixfold coordinated Si in SiO_2 glass at ultrahigh pressures. Proceedings of the National Academy of Sciences, 114(38), 10041-10046.

Salmon, P.S., Moody, G.S., Ishii, Y., Pizzey, K.J., Polidori, A., Salanne, M., Zeidler, A., Buscemi, M., Fischer, H.E., and Bull, C.L. (2019) Pressure induced structural transformations in amorphous $MgSiO_3$ and $CaSiO_3$. Journal of Non-Crystalline Solids: X, 3, 100024.

Sanchez-Valle, C., and Bass, J.D. (2010) Elasticity and pressure-induced structural changes in vitreous $MgSiO_3$-enstatite to lower mantle pressures. Earth and Planetary Science Letters, 295(3-4), 523-530.

Sen, S., Maekawa, H., and Papatheodorou, G.N. (2009) Short-Range Structure of Invert Glasses along the Pseudo-Binary Join $MgSiO_3$−Mg_2SiO_4: Results from 29Si and 25Mg MAS NMR Spectroscopy. The Journal of Physical Chemistry B, 113(46), 15243-15248.

Shen, G., Mei, Q., Prakapenka, V.B., Lazor, P., Sinogeikin, S., Meng, Y., and Park, C. (2011) Effect of helium on structure and compression behavior of SiO_2 glass. 108(15), 6004-6007.

Shim, S.-H., and Catalli, K. (2009) Compositional dependence of structural transition pressures in amorphous phases with mantle-related compositions. Earth and Planetary Science Letters, 283(1-4), 174-180.

Sinogeikin, S., Bass, J., Prakapenka, V., Lakshtanov, D., Shen, G., Sanchez-Valle, C., and Rivers, M. (2006) Brillouin spectrometer interfaced with synchrotron radiation for simultaneous x-ray density and acoustic velocity measurements. Review of Scientific Instruments, 77(10), 103905.

Speziale, S., Zha, C.-S., Duffy, T.S., Hemley, R.J., and Mao, H.-k. (2001) Quasi-hydrostatic compression of magnesium oxide to 52 GPa: Implications for the pressure-volume-temperature equation of state. Journal of Geophysical Research, 106(B1), 515-528.

Stolen, R.H., Krause, J.T., and Kurkjian, C.R. (1970) Raman scattering and far infra-red absorption in neutron compacted silica. Discussions of the Faraday Society, 50(0), 103-107.

Suzuki, I., Anderson, O.L., and Sumino, Y. (1983) Elastic properties of a single-crystal forsterite Mg_2SiO_4, up to 1,200 K. Physics and Chemistry of Minerals, 10(1), 38-46.

Wang, Y., Sakamaki, T., Skinner, L.B., Jing, Z., Yu, T., Kono, Y., Park, C., Shen, G., Rivers, M.L., and Sutton, S.R. (2014) Atomistic insight into viscosity and density of silicate melts under pressure. Nature Communications, 5(1), 3241.

Wojdyr, M. (2010) Fityk: a general-purpose peak fitting program. Journal of Applied Crystallography, 43(5-1), 1126-1128.

Xue, X., Stebbins, J., Kanzaki, M., McMillan, P., and Poe, B.J.A.M. (1991) Pressure-induced silicon coordination and tetrahedral structural changes in alkali oxide-silica melts up to 12 GPa: NMR, Raman, and infrared spectroscopy. 76, 8-26.

Yokoyama, A., Matsui, M., Higo, Y., Kono, Y., Irifune, T., and Funakoshi, K.-i. (2010) Elastic wave velocities of silica glass at high temperatures and high pressures. Journal of Applied Physics, 107(12), 123530.

Yu, T., Prescher, C., Ryu, Y.-J., Shi, F., Greenberg, E., Prakapenka, V., Eng, P., Stubbs, J., Kono, Y., and Shen, G. (2019) A Paris-Edinburgh Cell for High-Pressure and High-Temperature Structure Studies on Silicate Liquids Using Monochromatic Synchrotron Radiation. Minerals, 9(11), 715.

Figure Captions

Figure. 1 Raman spectra of $MgSiO_3$ glass. (A) Raman spectra of $MgSiO_3$ glass during compression to 67 GPa (red asterisks indicate positions where new peaks emerged). (B) Spectra during decompression to ambient pressure. (C) Deconvoluted Raman spectra up to 8 GPa (red arrows indicate reduction in intensities of the "defect peak" (magenta dashed lines), which is related to n-membered rings upon pressure increase).

Figure. 2 Multifaceted integrated plots of $MgSiO_3$ glass at ambient temperature (300 K). (A) Pressure dependent Raman peak shifts up to 67 GPa. Solid and open diamonds are data during compression and decompression, respectively. Red solid symbols are the new Raman

852 bands appearing upon increasing pressure. Red open symbols are the new Raman peak positions
853 during decompression. Lines are a guide to the eye. (B) Position of FSDP as a function of
854 pressure during compression. Note a large jump at 8 GPa. (C) Positions of r_{Si-O} obtained from
855 g(r), upon compression, by deconvoluting the assigned peaks with Gaussian functions. Red solid
856 circles and blue empty diamonds correspond to results with and without applying the Lorch
857 modification function, respectively. (D) Positions of deconvoluted $r_{(Si-Si)}$ obtained from g(r),
858 upon compression. Symbols are the same as in (C). (E) Bond angles of ∠Si-O-Si with (red solid
859 circle) and without (blue empty diamond) using Lorch modification function and ∠O-Si-O (black
860 empty diamond). (F) Compressional (V_p) and shear wave (V_s) velocities measured by Brillouin
861 scattering. Solid blue and red circles (V_p) with diamonds (V_s) are the 1^{st} and 2^{nd} runs,
862 respectively. Red (hot compression) and black (cold compression) dashed lines represent
863 pressure dependencies of V_p and V_s based on MD simulations (Ghosh et al., 2014), respectively.
864

865 **Figure. 3 Angle Dispersive X-ray scattering data up to 72 GPa.** (A) Experimental structure
866 factor S(Q). The corresponding pressure values are indicated on the right. (B) g(r). Red dotted
867 lines are results without applying the Lorch function. Black lines are results with Lorch function
868 applied. Ripples due to truncation in Q range are minimized in this case, but some fine features
869 are also lost for g(r).

870 **Figure. 4 Proposed mechanisms of structural evolution in $MgSiO_3$ glass.** (A) The 6-, 5-, 4-
871 membered rings and chain structures dominated by Q^2 species at ambient conditions. (B)
872 Monomers and dimers bind with available Q^0 and Q^1 species, resulting in an increase in
873 concentration of Q^1 and Q^2 species, respectively. Size of n-membered rings is reduced to n = 4-,
874 3- with increasing chain interconnectivity. The Mg^{2+}, "counter cation", acts as a stabilizer in

875 $MgSiO_3$ glass. (C) Distortion increases within 4-, 3-membered rings with pressure and forms
876 oxygen tri-clusters (regions shaded with pale red). The arrows indicate the displacement of the Si
877 and O atoms as the structure is compressed. (D) Above 8 GPa, the oxygen tri-clusters
878 concentration increases, so that Si becomes pseudo penta-coordinated (pale blue). (E)
879 Tetrahedral Q^n species diminish due to structural modification. Concentration of pentahedrally
880 coordinated SiO_5 (pale blue) increases, and octahedrally coordinated SiO_6 (dark red) forms above
881 20 GPa. Mg-O_y (y>4.5) polyhedral begin to bind with nearest structural units, increasing Mg
882 coordination number (CN). (F) Pentahedrally coordinated SiO_5 undergoes more distortion,
883 increasing the concentration of edge-sharing octahedral SiO_6 units as well as CN of Mg, towards
884 6 or even 8.

885

886 **Figure. 5 Comparison of selected bond-lengths for SiO_2, $MgSiO_3$, and Mg_2SiO_4 glasses.** (A)
887 Pressure dependence of the Si-O bond distance in $MgSiO_3$ with (red solid circles) and without
888 (blue empty diamonds) using the Lorch modification function, MD simulation of $MgSiO_3$ (red
889 dashed line), SiO_2 (black solid circles), and Mg_2SiO_4 (orange squares) glasses. (B) Pressure
890 dependence of the Mg-O bond distance in $MgSiO_3$ glass without using the Lorch modification
891 function (blue empty diamonds), MD simulation of $MgSiO_3$ (red dashed line) and Mg_2SiO_4
892 (orange solid squares) glasses. References are given in the plots.

893

This is the peer-reviewed, final accepted version for American Mineralogist, published by the Mineralogical Society of America.
The published version is subject to change. Cite as Authors (Year) Title. American Mineralogist, in press.
DOI: https://doi.org/10.2138/am-2022-7969. http://www.minsocam.org/

Table 1. Distribution of Q^n species (%) of $MgSiO_3$ glass at 1 Bar at room temperature, using different experimental methods.

Q^0	Q^1	Q^2	Q^3	Q^4	Density (g/cc)	P, T Condition	Method	Ref.
0.0	25	42	25.7	7.3	--	0 GPa, ≤1850 K	^{29}Si NMR	(1)
1.4(1)	19.1(3)	53.0(4)	25.2(3)	1.4(1)	--	0 GPa, ≤1850 K	^{29}Si NMR	(2)
11.4(6)	23.7(2)	32.5(3)	32.4(3)	0	--	0 GPa, ≤1850 K	Raman	(3)
15(4)	30(5)	35(5)	20(4)	0	2.774	≤1 GPa, ≤2000 K	Raman	This Study
7.2	20.5	41.4	24.8	6.1	2.730	0 GPa, 3000 K	MD	(4)
7.1	20.0	24	28.8	20.1	2.800	0 GPa, 2000 K	MD	(5)
7	21	28	31	12	2.620	0 GPa, 3000 K	MD	(6)
4(1)	24(3)	44(6)	25(2)	4(2)	2.635	0 GPa, ≤2430 K	AIM MD	(7)

References: (1) Sen et al., 2009; (2) Davis et al., 2011; (3) Kalampounias et al., 2009; (4) Kubicki and Lasaga, 1991; (5) Shimoda and Okuno, 2006; (6) Ghosh et al., 2014; (7) Salmon et al., 2019.

Table 2. Structural and physical properties of SiO_2, $MgSiO_3$, and Mg_2SiO_4 glasses.

Glass	NBO/T[(a)]	Mg-O CN[(b)]	$r_{Mg\text{-}O}$[(c)]	Cavity[(d)]	T_m[(e)]	ρ_0,	K_{T0}[(f)]	K'_{T0}[(g)]
	--	--	Å	%	K	g/cm^3	GPa	--
SiO_2	0	--	--	30.9[(7)]	1984	2.20[(1)]	36.4[(2)]	-2.66[(2)]
$MgSiO_3$	2	4.5[(3)]	1.99, 2.21[(3)]	3.1[(7)]	1853[(4)]	2.77[(5)]	16.9[(5)]	+5.9[(5)]
Mg_2SiO_4	4	5.0-5.5[(4)]	2.0[(4)]	0[(7)]	2163[(4)]	2.93[(6)]	100[(8)]	+1[(8)]

Notes:

[(a)] Average number of non-bridging oxygen (NBO) per tetrahedron, based on compound formulas.

[(b)] Average coordination number of Mg at ambient pressure. CN of Mg increases to~6.6 at ~30 GPa for Mg_2SiO_4 glass (Benmore et al., 2011).

[(c)] Average Mg-O bond distance. Two distinct Mg-O distances are observed in neutron diffraction with isotropic substitution (Cormier and Cuello, 2011) for $MgSiO_3$ glass. Mg-O distance decreases slightly from 2.0 to ~1.9 Å at ~30 GPa for Mg_2SiO_4 glass (Benmore et al., 2011).

[(d)] Cavity concentrations in the glasses are based on reverse Monte-Carlo calculations (Kohara et al., 2011).

[(e)] Melting points at ambient pressure.

[(f)] Isothermal bulk modulus was obtained from static compression experiments.

[(g)] Pressure derivatives of the isothermal bulk moduli is based on equation-of-state fit to compression data. Note negative K'_{T0} for SiO_2 glass.

Superscript number indicates references: [(1)] Yokoyama et al., 1987; [(2)] Kono et al., 2011; [(3)] Cormier and Cuello, 2011; [(4)] Benmore et al., 2011; [(5)] Petitgirard, 2017; [(6)] Kohara et al., 2004; [(7)]Kohara et al., 2011; and [(8)] Lesher et al., 2009.

This is the peer-reviewed, final accepted version for American Mineralogist, published by the Mineralogical Society of America.
The published version is subject to change. Cite as Authors (Year) Title. American Mineralogist, in press.
DOI: https://doi.org/10.2138/am-2022-7969. http://www.minsocam.org/

Figure 1.

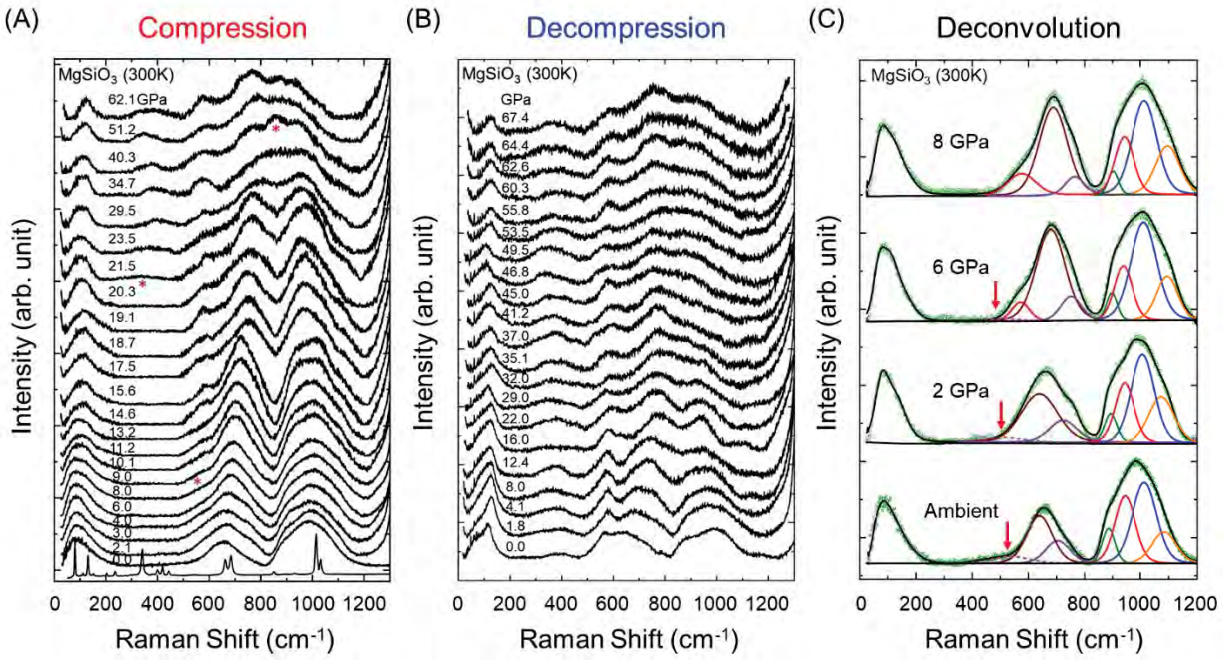

This is the peer-reviewed, final accepted version for American Mineralogist, published by the Mineralogical Society of America.
The published version is subject to change. Cite as Authors (Year) Title. American Mineralogist, in press.
DOI: https://doi.org/10.2138/am-2022-7969. http://www.minsocam.org/

Figure 2.

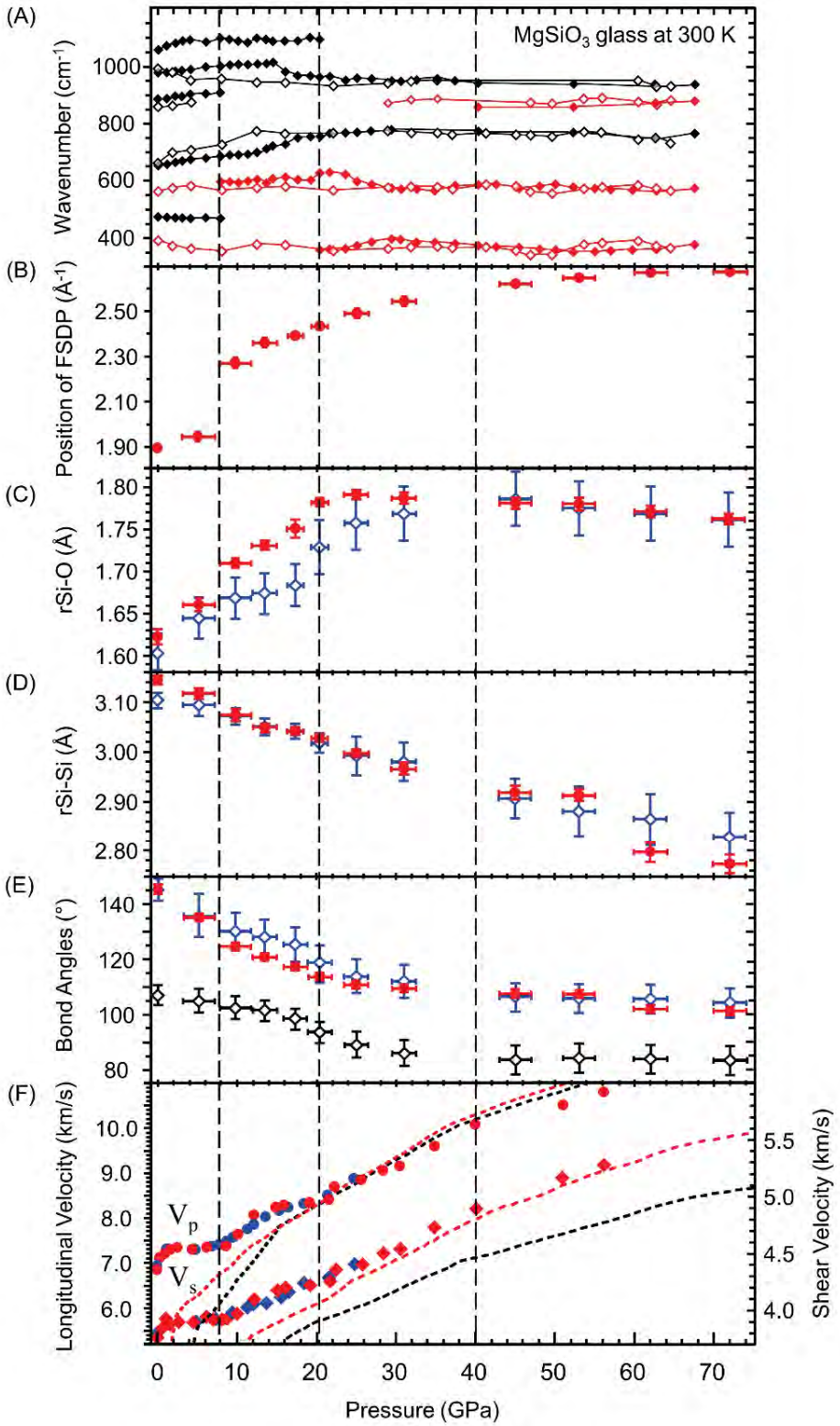

This is the peer-reviewed, final accepted version for American Mineralogist, published by the Mineralogical Society of America.
The published version is subject to change. Cite as Authors (Year) Title. American Mineralogist, in press.
DOI: https://doi.org/10.2138/am-2022-7969. http://www.minsocam.org/

Figure 3.

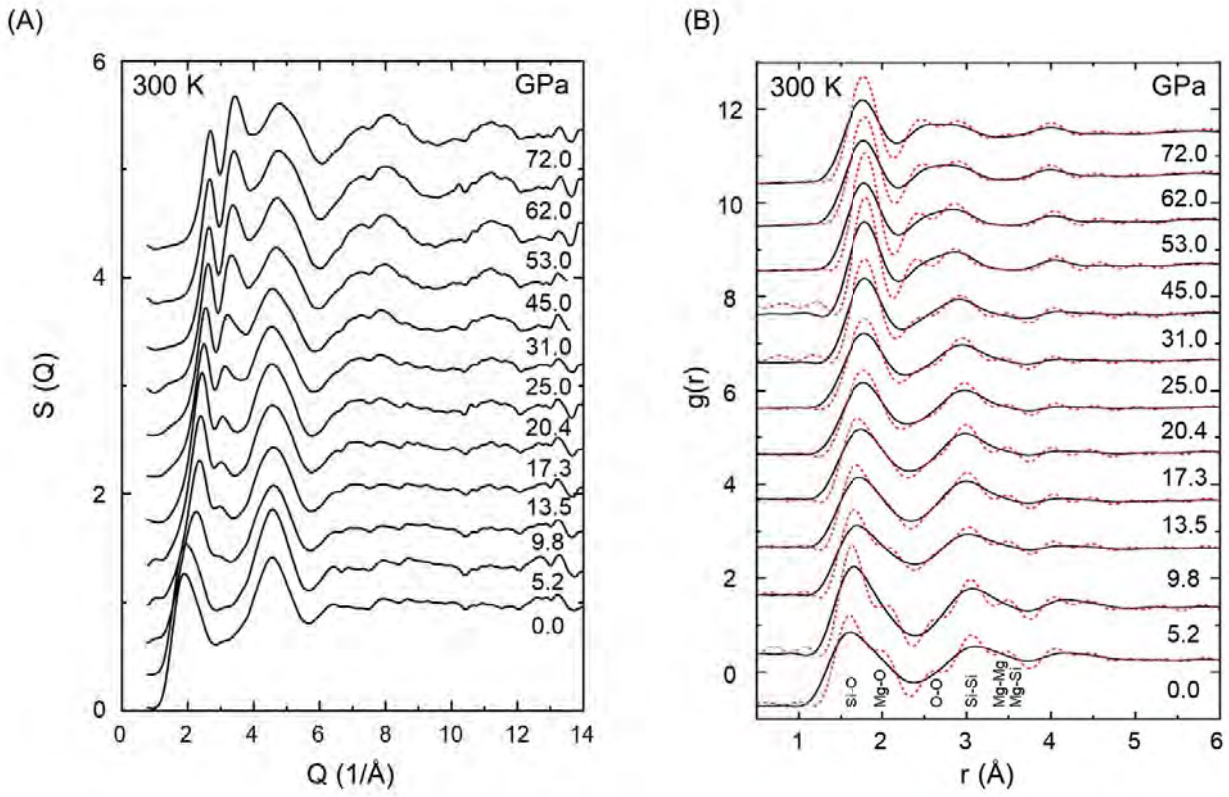

This is the peer-reviewed, final accepted version for American Mineralogist, published by the Mineralogical Society of America.
The published version is subject to change. Cite as Authors (Year) Title. American Mineralogist, in press.
DOI: https://doi.org/10.2138/am-2022-7969. http://www.minsocam.org/

Figure 4.

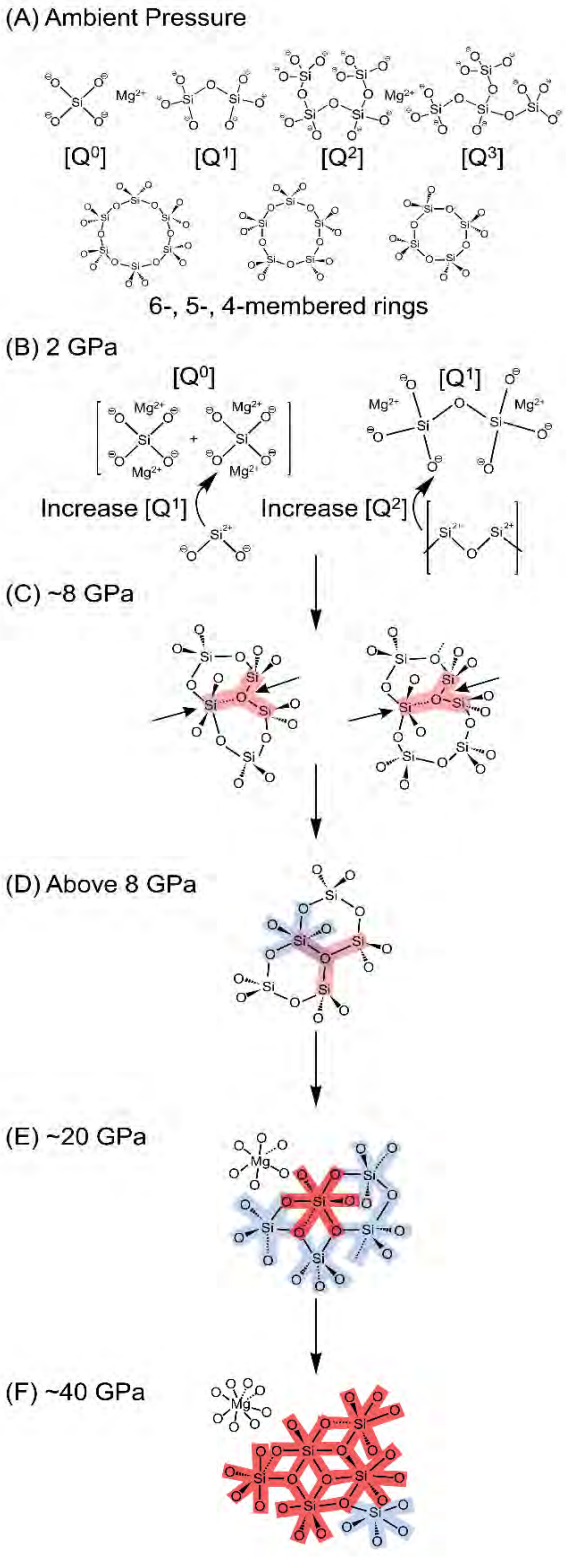

This is the peer-reviewed, final accepted version for American Mineralogist, published by the Mineralogical Society of America.
The published version is subject to change. Cite as Authors (Year) Title. American Mineralogist, in press.
DOI: https://doi.org/10.2138/am-2022-7969. http://www.minsocam.org/

Figure 5.